Nano Research

ISSN 1998-0124 CN 11-5974/O4
https://doi.org/10.1007/s12274-019-2425-5

Research Article

Nanoscale imaging of electric pathways in epitaxial graphene nanoribbons

Johannes Aprojanz[1,2], Pantelis Bampoulis[2,3], Alexei A. Zakharov[4], Harold J. W. Zandvliet[3], and Christoph Tegenkamp[1,2] (✉)

[1] *Institut für Physik, Technische Universität Chemnitz, Chemnitz 09126, Germany*
[2] *Institut für Festköperphysik, Leibniz Universität Hannover, Hannover 30167, Germany*
[3] *Physics of Interfaces and Nanomaterials, MESA+ Institute for Nanotechnology, University of Twente, Enschede 7522 NH, The Netherlands*
[4] *MAX IV Laboratory and Lund University, Lund 22100, Sweden*

Received: 4 February 2019 / **Revised:** 22 March 2019 / **Accepted:** 27 April 2019

ABSTRACT

Graphene nanoribbons (GNRs) are considered as major building blocks in future carbon-based electronics. The electronic performance of graphene nanostructures is essentially influenced and determined by their edge termination and their supporting substrate. In particular, semi-conducting, as well as metallic GNRs, can be fabricated by choosing the proper template which is favorable for device architecture designs. This study highlights the impact of microscopic details of the environment of the GNRs on the charge transport in GNRs. By means of lateral force, conductive atomic force and nanoprobe measurements, we explore the charge propagation in both zig-zag and armchair GNRs epitaxially grown on SiC templates. We directly image transport channels on the nanoscale and identify SiC substrate steps and nano-instabilities of SiC facets as dominant charge scattering centers.

KEYWORDS

sidewall graphene nanoribbons, nanoprobe, conductive-AFM, nanoscale transport

1 Introduction

The current progress in growth and processing techniques of epitaxial graphene makes it a superior contender for applications in nanoelectronics [1–5]. Especially the utilization of these techniques in the fabrication of 1D nanostructures, e.g., graphene nanoribbons (GNRs) grown by selective sublimation on sidewalls of mesa structures etched in 6H-SiC results in edge specific atomically precise nanowires with extraordinary structural and electronic quality [6]. However, this high-temperature growth approach is often accompanied by non-uniform step-flow and debunching of vicinal SiC surfaces, which directly influences the electronic properties of epitaxial graphene nanoribbons.

Recently, the suppression of debunching in sidewalls aligned parallel to the $[1\bar{1}00]$ direction of SiC was reported resulting in microscopically smooth facets. These facets serve as an ideal template to produce GNRs that display room temperature ballistic transport on the µm-scale with a quantized conductance of e^2/h [7–9].

These flawless sidewall configurations require precise control of alignment and growth conditions, i.e., SiC nano-facets tend to suffer from instabilities. Nanowires grown in the perpendicular $[11\bar{2}0]$ direction revealed a nanorippling of the graphene, which was predetermined by the underlying facets. In these periodic mini-ribbon arrays, band gap openings were observed, thus exhibiting an entirely different electronic behavior compared to GNRs grown in the $[1\bar{1}00]$ direction [10, 11]. In both cases the termination of the edges and the morphology of the sidewall influence and determine the electronic properties of the corresponding GNRs.

The integration of GNRs in future carbon-based nanoelectronics demands a profound understanding of charge transport in these nanostructures as well as the identification of defects and interactions with the substrate, which crucially limit the propagation of charge carriers. Conductive atomic force microscopy (c-AFM) is the method of choice to address the influence of roughness and nano-instabilities on electric performance due to the simultaneous acquisition of morphological and electronic information on the nanoscale [12–14]. The correlation of direct high-resolution visualization of electric tracks with established transport studies on epitaxially grown GNRs will contribute to control and design future carbon-based electronics.

In this work, the combination of high-resolution lateral force microscopy (LFM), conductive AFM and local nanoprobe transport is used to explore nanoscale transport channels in zig-zag (zz) and armchair (ac) GNRs. We have directly imaged a single conductive channel, located at the bottom edge of a zz-GNR, and confirmed its ballistic nature by probe spacing dependent nanoprobe measurements. Nano-faceting was observed for ac-GNRs. By application of two different c-AFM modes, we have assigned suspended GNRs at step edges and zero layer formation on flat SiC nanoterraces. Finally, the metallic and semi-conducting transport characteristics of zz- and ac-GNRs were explored by local IV curves.

2 Experimental

Semi-insulating 6H-SiC wafers (II-VI Germany GmbH) were used as a template to produce 25 nm high mesa structures by means of optical lithography and reactive ion etching (RIE). The mesa structures were defined along the $[1\bar{1}00]$ (zig-zag, zz) and the $[11\bar{2}0]$ (armchair, ac) directions of the SiC(0001) sample. Graphene growth was done in a semi-closed inductive RF-furnace at 2,000 °C in 1 bar Argon atmosphere [15, 16]. Additional details about the growth and

Address correspondence to christoph.tegenkamp@physik.tu-chemnitz.de

characterization of as-grown GNRs are provided in [8, 17, 18].

Conductive AFM (c-AFM) experiments were performed with an Agilent 5100 AFM in contact mode with diamond (AD-E-0.5-SS Adama Innovations Ltd., 0.003–0.005 Ω·cm, spring constant: 0.5 N/m, resonance frequency 30 kHz) and Pt tips (12Pt400B Rocky Mountains, spring constant: 0.3 N/m, resonance frequency: 4.5 kHz) in N_2 environment. Based on the Hertz model the calculated contact area of the diamond tip is 0.5 ± 0.2 nm^2 and 3 ± 1 nm^2 for the Pt tip. Thereby, both so-called vertical and lateral transport modes were used, see Figs. S1(a) and S1(b) in the Electronic Supplementary Material (ESM). In the former, the SiC is directly contacted with Ag-paint. In the latter, a flake of graphite mechanically applied on top of the GNRs of interest was used as the second electrode. This choice ensured the proper placement of the second electrode on top of the GNRs. In all cases, the voltage was applied to the second large electrode directly connected to the sample, i.e., SiC in the vertical mode and the graphite flake in the lateral mode, while the tip was grounded. Local transport measurements were carried out using a commercial Omicron 4-tip scanning tunneling/scanning electron microscope (STM/SEM) operating under ultrahigh-vacuum (UHV) conditions, which is additionally equipped with a spot profile analysis-low energy electron diffraction (SPA-LEED) system. A Gemini type SEM was used for precise navigation and positioning of the electrochemically etched W tips with apex radii of 20–70 nm.

3 Results and discussion

3.1 Large-scale characterization of GNR arrays

We start with the large-scale characterization of as-grown GNR arrays on SiC mesa structures oriented along the [1$\bar{1}$00] direction. The facets of the mesa structures have a slope of about 20–30° with respect to the (0001) plane and host 40–50 nm wide GNRs [7, 18]. Figure 1(a) shows a SPA-LEED image acquired from a 600 μm^2 sampling area (size of the electron beam). The pattern exhibits the characteristic ($6\sqrt{3} \times 6\sqrt{3}$) and (6 × 6) reconstruction spots indicating that the planar surface is homogeneously covered by a semi-conducting zero layer [19]. Moreover, the intensity of the first order diffraction spots of graphene (black arrow) is weak as compared to SiC (blue arrow) further supporting the formation of zero layer graphene. The intensity originating from the sidewalls is limited by the coverage below 5% of a monolayer, hence diffraction spots from the facets were not detected.

To further explore the sidewalls, we have done comprehensive lateral force microscopy measurements. The signal of a lateral force image represents the torsion of the cantilever that arises from frictional forces between the surface and the tip. We would like to note here that the choice of LFM over conventional AFM topography is justified by the higher sensitivity of the lateral force signal as compared to topography to surface variations [20], which is evident in the atomic scale lateral force image shown in Fig. 1(b). The LFM image was acquired on a sidewall and reveals a periodicity of about 0.25 nm, i.e., the periodicity of the graphene lattice supporting the selective growth of graphene on SiC sidewalls.

Figure 1(c) shows the trace (left to right) lateral deflection image of a GNR array. As our LFM measurements were done on vicinal surfaces, the lateral component of the cantilever load normal to the surface needs to be taken into account [21]. Each mesa structure hosts two sidewalls with opposite slopes, thus the cantilever moves uphill and downhill, respectively. Accordingly, an alternating LF signal is expected only if the topography causes the lateral deflection. In Fig. 1(d), the extracted line-profiles exhibit a similar lateral deflection on each sidewall, but in addition, a clear change of LF contrast is conspicuous in the trace and the retrace direction, showing that the tip interacts with a different material than on the rest of the surface.

Moreover, the simultaneously recorded c-AFM image depicted in Fig. 1(e) further confirms the presence of electronically isolated GNRs. As is obvious from the current image, the locations of GNRs, i.e., the facets of the mesa structure, are significantly more conductive than the planar surface. Figure 1(f) compares the signals obtained in lateral force imaging and current imaging. The measured cross sections clearly reveal that the current originates from the locations with a distinct contrast in lateral force, precisely at the sidewalls of the mesa structures. Noteworthy, substrate steps of SiC running perpendicular to the mesa structures show a clear signal both in lateral force and current images. These ribbons grown on natural SiC steps (see arrows in Fig. 1(c)) eventually interconnect two sidewalls of the mesa structure. It is well-known that atomic steps serve as seeds for graphene nucleation and thus parasitic graphene growth is hardly avoidable [22]. Nonetheless, the epitaxially grown GNRs run (almost) uninterrupted for micrometers, unambiguously demonstrating a high-quality large scale growth of electronically isolated nanowires.

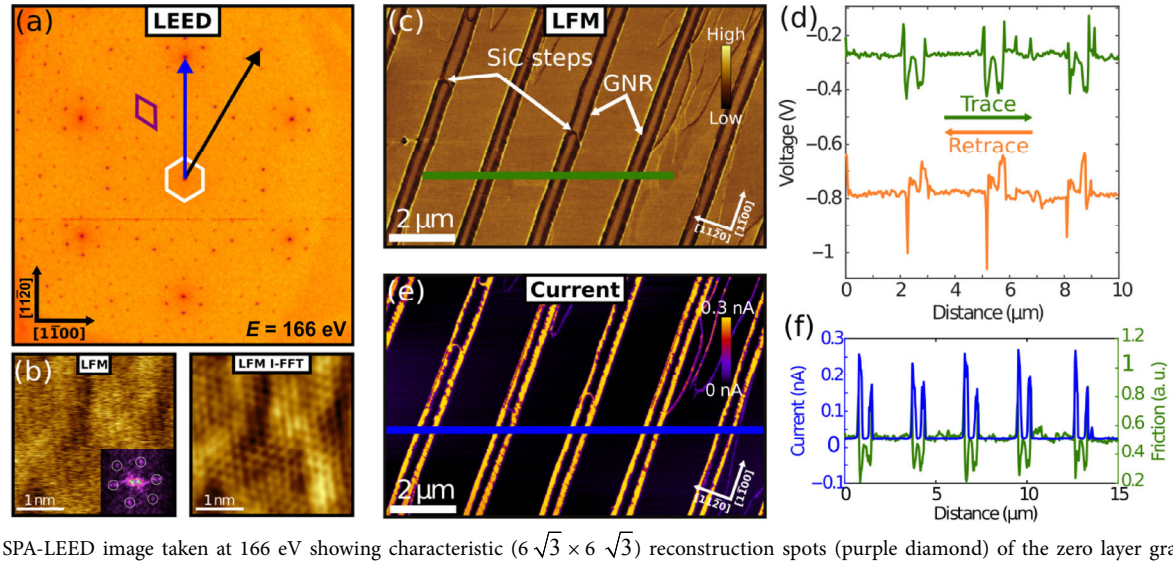

Figure 1 (a) SPA-LEED image taken at 166 eV showing characteristic ($6\sqrt{3} \times 6\sqrt{3}$) reconstruction spots (purple diamond) of the zero layer graphene on SiC. Additionally, the first order diffraction spots of graphene (black arrow) and SiC (blue arrow) as well as the (6 × 6) reconstruction (white hexagon) are highlighted. (b) Atomic scale LFM image of a GNR showing a periodicity of 0.25 nm. For better clarity a Fourier-filtered image is provided. The slight distortion of the graphene lattice originates from instrumental drift. (c) Trace lateral force microscopy image of an zz-GNR array. (d) Extracted line-profiles from trace and retrace LFM images. (e) Simultaneously taken current image of the GNR array. Sample bias: 5 mV. (f) Overlayed line-scans comparing current and friction signals.

3.2 Zig-zag GNR

The c-AFM image of Fig. 2(a), recorded on a facet oriented along the [1$\bar{1}$00] direction demonstrates that the current exclusively flows in the zz-GNR. At its lower part, a 6–7 nm wide, low resistance current path is captured to run uninterruptedly for hundreds of nanometers. The central and top parts of the GNR show a noisier current signal. In order to explore whether this transport channel arises from instabilities of the underlying facet or from inhomogeneities on the surface of the GNR, high-resolution LFM measurements and two modes of c-AFM, i.e., vertical and lateral transport (see Fig. S1 in the ESM), were used. The LFM image in Fig. 2(b) shows that the GNR is morphologically flat. Besides some small roughness no significant topographic features, like nanofacets were detected. Interestingly, the bottom channel appeared only when the GNRs were contacted by the graphite electrode (lateral transport), cf. Figs. 2(b) and 2(c). The difference in the appearance of the zz-GNR in the two transport modes can be explained by considering the difference of the charge injection mechanism between the two modes. In the case of vertical transport, the GNR is contacted directly with the AFM tip while the second electrode contacts the SiC substrate. Here the GNR can be considered as a barrier sheet or buffer layer in between the SiC and the AFM tip. Graphene as a buffer layer was investigated in the field of semiconductors [23–25]. In such van der Waals bonded buffer layers the metal/graphene/semiconductor junction exhibits ambipolar transport and often ohmic characteristics. In particular, graphene reduces or alleviates the Schottky barrier height due to the depinning of the Fermi level as a result of the metal-induced gap states (MIGS) [26]. In contrast, in the parallel transport configuration both ends of the GNR are contacted directly, one by the AFM tip and the other by the graphite flake placed on top of the ribbon, which is a scenario similar to experiments using a nanoprobe system, where two metallic W tips are placed on the GNR and directly couple to its transport modes [18, 27].

The structural perfection and the absence of the edge channel while measuring through the substrate (vertical transport) clearly shows that it is an intrinsic transport property of the GNR originating from its electronic structure rather than the result of morphology. The LFM/c-AFM study reveals that the bulk parts of the zz-GNR are not interacting with the underlying SiC facet supporting the structural model of suspended GNRs. In addition, the appearance of the transport channel at the lower edge of the GNRs is in excellent agreement with our previous nanoscale transport studies of ballistic tracks and consistent with experiments across nanoconstrictions demonstrating robust transport through edge modes [9, 28]. Hence, only imperfections of the edges can severely impact and limit charge propagation.

We have combined c-AFM with 4PP-STM and SEM in UHV to explore in detail the electronic transport properties of GNRs. In contrast to c-AFM, in which air-borne contamination and large series resistances due to the van der Waals gap between the graphite flake (second electrode) and the GNR can alter the measured resistance, 4PP-STM with electronically invasive tips probes solely the intrinsic resistance of the GNR [29].

Nevertheless, as it is obvious from Fig. 3(a) the IV-characteristics recorded with both the c-AFM (see inset) and the nanoprobe system (main panel) exhibit metallic behavior indicating the formation of ohmic contacts. The local IV-curves obtained by a linear four point-probe (4PP) arrangement with an equidistant probe spacing of 750 nm shown in Fig. 3(a) were exemplary collected on sidewalls with structural imperfections, e.g., parasitic monolayer graphene growth and kinks (purple and blue) and a flawless sidewall (orange), which was investigated by c-AFM in the previous discussion. The resistance extracted for a structurally homogeneous GNR of 28 kΩ ≈ h/e^2, i.e., the resistance quantum, denotes single channel ballistic conduction. The two imperfect sidewalls reveal a noticeably smaller 7 kΩ and higher 150 kΩ resistance value at the same channel length of 750 nm, respectively.

Figure 3(b) summarizes the probe spacing dependent transport measurements done on these three types of GNRs. First, we consider the purple data set (low resistance), which was measured on GNRs with additional monolayer graphene at the upper edge (see Fig. 3(c)). Such a parasitic monolayer growth is often accompanied by the formation of multilayer graphene on the sidewall. The resistance decreases linearly with decreasing channel length with the intercept at zero resistance. Both are clear characteristics of 1D diffusive transport [30]. From the extracted resistance per length R/L of 12 kΩ/μm, we calculate the sheet resistance ρ_s using the equation $\rho_s = (R/L)^*w$ = 1.2 kΩ/□, assuming an average width of 100 nm. This value is comparable to epitaxial graphene on SiC and other diffusive GNR systems [27, 31]. Hence, the charge transport is dominated by the parasitic graphene, which is also evident in the c-AFM image in Fig. S2(a) in the ESM. On contrary, the blue and the orange curves show an apparently different transport mechanism. The resistance displays an offset of h/e^2 at zero probe spacing, again indicating single channel ballistic transport. The resistance scaling of the flawless GNRs (orange data set, SEM image depicted in Fig. 3(d)) can be understood in the framework of the two-terminal Landauer-Büttiker formalism [32]. In the presence of multiple scatters, the resistance of a single channel ballistic conductor is expected to follow $R(L) = h/e^2\ (1 + L/\Lambda)$, where

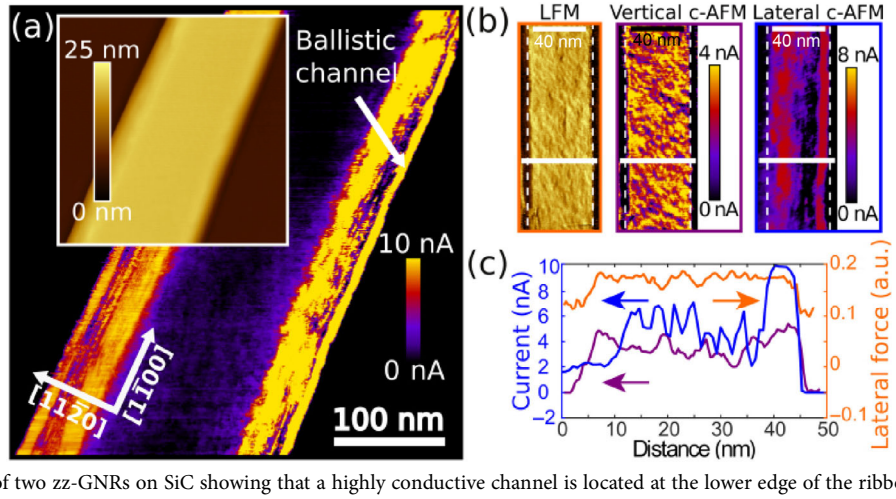

Figure 2 (a) Current image of two zz-GNRs on SiC showing that a highly conductive channel is located at the lower edge of the ribbons. Sample bias: 20 mV. Inset: Simultaneously acquired topography image. (b) Small scale lateral force (left) and current images of a zz-GNR recorded in vertical (middle panel) and lateral transport (right panel). (c) Extracted line-scans from images in (b). The lateral force image does not show any significant variations indicating that the GNR are structurally homogeneous. The bottom ballistic channel is solely visible in the lateral mode.

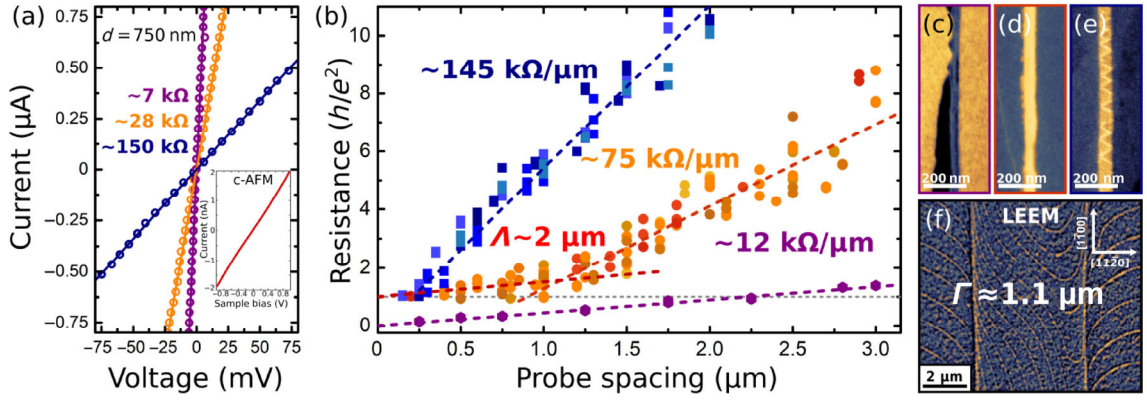

Figure 3 (a) IV-curves recorded in a four-point-probe configuration on three structurally different zz-GNRs at a fixed probe spacing of d = 750 nm. All zz-GNRs are clearly metallic as demonstrated by the linear IV-curves indicating ohmic behavior. The resistances extracted by linear fits yield 7, 28, and 150 kΩ. (b) Probe spacing dependent transport measurements performed on three different types of ribbons. The purple data set exhibits a linear increase with increasing probe spacing with an intercept of zero resistance characteristic for 1D diffusive conductors. The blue and orange curves (for each multiple GNRs were characterized) display a weakly linear spacing dependency with an offset resistance of h/e^2 up to 200 nm and 1 μm, respectively. For larger probe spacings a steep linear increase was detected. For clarity, channel lengths below 150 nm were not included due to the occurrence of bulk conduction channels. (c)–(e) SEM images of GNRs probed in (a) and (b). (f) LEEM image showing SiC substrate steps on mesa structures.

Λ is the electron mean free path. According to this model, we extract an electron mean free path of ≈ 2 μm. For probe spacing larger than 1 μm, the slope of the resistance dependence suddenly increases. We attribute this to a transition from the ballistic to the diffusive transport regime. Interestingly, this transition coincides with the average SiC terrace width Γ of 1.1 μm which was extracted from the low energy electron microscopy (LEEM) image in Fig. 3(f). During high-temperature growth surface diffusion leads to step-flow processes and hence the curved shape of the bunched SiC steps (height: 0.5–1 nm, see Fig. S3 in the ESM) originates from the so-called step wandering, which arises from pinning of the SiC steps at the sidewalls [33]. These pinning centers serve as strong scattering centers and therefore destroy long-range ballistic transport. Indeed, the shift of the transition to even smaller channel lengths of ≈ 200 nm (blue) can be understood in a similar picture. In Fig. 3(e) the SEM image shows a sidewall with regularly distributed kinks which easily occur due to small misalignment of the mesa structure during fabrication (see also Fig. S2(b) in the ESM). Thus, the GNR split by these nano-instabilities into effectively shorter GNRs. This is also reflected in the resistance per length in the diffusive regime, which yields ≈ 145 kΩ/μm, almost twice as large as in the flawless case ≈ 75 kΩ/μm. However, the ballistic nature of charge propagation is still preserved in these GNR segments, which is strongly supported by the observation of quantized conduction plateaus for probe spacings below 150 nm (see Fig. S4 in the ESM).

As demonstrated, the electronic properties and especially the ballistic transport channel of zz-GNRs crucially depend on structural details of the environment which reconfirms the need for a superior control over growing conditions. In general, the family of $(11\bar{2}n)$ facets, which host the exceptional zz-GNRs tends to decompose into nano-facets with energetically more favorable orientations. Commonly such nano-faceted sidewalls exhibit facets of both families, i.e., armchair $(1\bar{1}0n)$ and zigzag $(11\bar{2}n)$ [34]. In the following, we will focus on sidewalls oriented parallel to the $[11\bar{2}0]$ direction.

3.3 Armchair GNR

GNRs grown on facets aligned along the $[11\bar{2}0]$ direction were shown to be armchair terminated [10]. A c-AFM image of such an ac-GNR is depicted in Fig. 4(a), the inset corresponds to the topography. In contrast to the zz-GNRs, the ac-GNRs show a current modulation with a periodicity of 3–5 nm running across the GNR. The modulation arises from the nano-faceting of the SiC mesas during growth. This process results in the splitting of the sidewall into smaller terraces of full-unit cell height of 6H-SiC [8, 35]. As can be seen in Fig. 4(b), the lateral force image of an ac-GNR shows well-defined stripes running parallel to the ribbon. These narrow and long stripes are directly reflected in the distinct current modulation shown in the right panel of Fig. 4(b). The conductivity of the ac-GNR was again explored in two modes as described in the experimental section. The current image in Fig. 4(b) corresponds to the measurement done in the vertical mode. Figure 4(d) shows the corresponding cross sections taken across the ribbon on both the current and the lateral force image. The cross section reveals that in both images the periodic patterns are in-phase with each other. As obvious, in this configuration, the terraces of the nano-facets on ac-GNRs are more conductive than their edges. This could be understood by considering bond formation between the graphene and the SiC(0001) surface at these planar locations. In the zero layer, approximately every third carbon atom is bonded to the SiC substrate leading to an increased tunneling probability and therefore to an enhancement of the current signal at strongly coupled regions. Contrary, at the edges of the nano-facets, the graphene delaminates from SiC forming quasi-freestanding GNRs [11]. We attribute the lower conductivity to the formation of a van der Waals gap between the GNR and SiC at weakly coupled regions [23].

This model is further supported by measurements done in the lateral transport configuration. The detected modulation in the current image gets out-of-phase with the terraces in the friction image when the GNRs were directly contacted by a graphite flake, Figs. 4(c) and 4(e). In the lateral mode, the decoupled quasi-freestanding regions are the most conducting, since at these locations the delamination preserves the metallic properties of graphene. At regions where the coupling is stronger, hybridization with the underlying substrate leads to gap opening, hence to lower conductivity. Thus, the differences in the charge transport and characteristics of the ac-GNR for the lateral and vertical transport directions are the result of this coupling modulation of the ac-GNR and the SiC facet.

This is also captured by the c-AFM IV-spectroscopy. Figure 5 depicts IV-curves recorded on ac-GNRs on top of the edges and the nano-terraces in both transport configurations. In both cases, the current is lower compared to zz-GNRs. More importantly, the IV-characteristics are non-linear and resemble those of a metal-semiconductor nanojuction, confirming the semi-conducting properties of the ac-GNR. The lower conductivity of the ac-GNR in the vertical mode as compared to the lateral mode, naturally arises from the differences of the two junctions, i.e., metal/SiC/ac-GNR/tip and graphite/ac-GNR/tip.

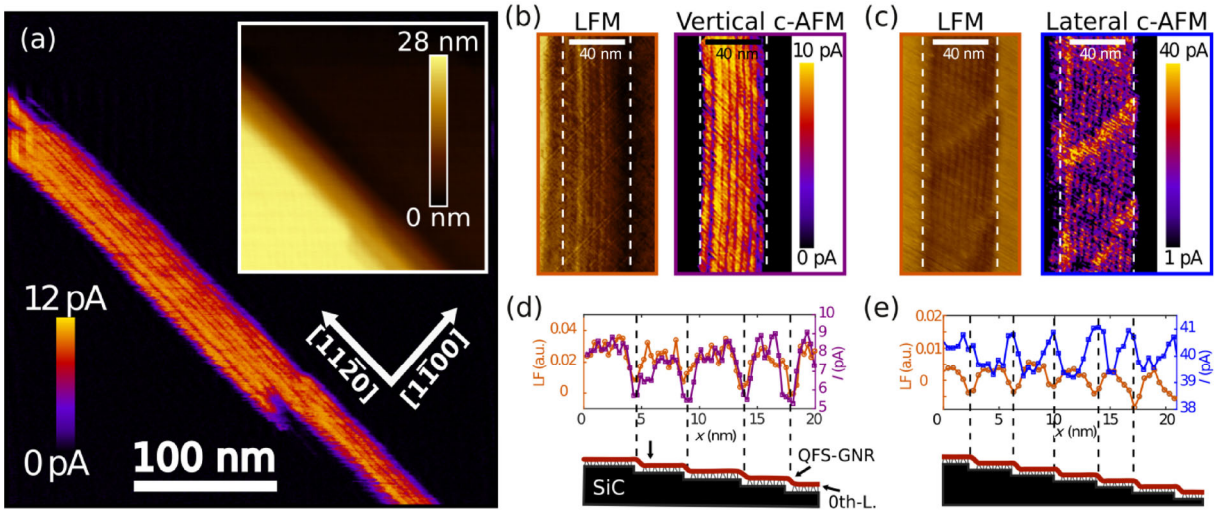

Figure 4 (a) Current image of an ac-GNR obtained with a sample bias of 0.9 V, a modulation of about 5 nm is observed. Inset: the corresponding topography. (b) Small scale lateral force (left) and current (right) images of the GNR in (a). The modulation in the current image is in-phase with the modulation in the lateral force image. The lower levels in the lateral force image are attributed to steps in the SiC mesa, whilst the brighter parts to small terraces. When scanning in vertical configuration, the terraces are more conductive than the steps. This is also shown in the cross sections of panel (d). In contrast, when scanning in lateral mode, the steps are more conductive than the terraces, which can be seen in both the current image (sample bias 0.9 V) of panel (c) and the corresponding cross sections of panel (e) of the lateral force and current images that are clearly out-of-phase. The images were taken close to the ac-GNR in (b).

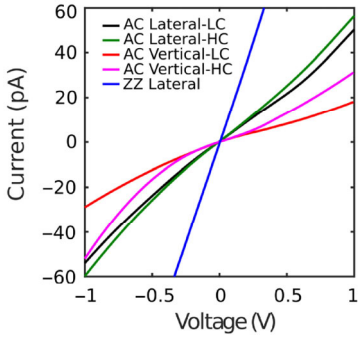

Figure 5 IV curves collected in both, lateral and vertical transport by c-AFM. zz-GNR reveal a metallic IV characteristic while ac-GNR are clearly non-linear. LC and HC indicates low and high conductance, respectively.

4 Conclusions

Based on detailed LFM, c-AFM and *in-situ* nanoprobe measurements, we have confirmed the selective growth of electronically well-isolated graphene nanoribbons on SiC sidewalls. Nanoscale transport channels were directly imaged in both zig-zag and armchair GNRs. We have identified a ~ 6 nm wide transport channel located at the lower edge of metallic zz-GNR and showed its ballistic nature by local transport measurements. The charge carrier propagation in this edge channel is significantly limited by natural substrate steps and nano-instabilities of the sidewalls. Armchair GNRs revealed semi-conducting transport characteristics originating from nano-faceting of the sidewall. The nano-faceting results in an array of mini-terraces which was reflected in a periodic modulation of the current signal in c-AFM measurements. By comparing vertical and lateral c-AFM current signals and considering charge carrier injection mechanisms between graphene/semiconductor interfaces, we could assign zero layer graphene to flat mini-terraces and suspended graphene to their step edges. This study highlights the importance of the impact of microscopic details on the electronic performance of GNRs.

Acknowledgements

J. A. and C. T. gratefully acknowledge financial support by the Deutsche Forschungsgemeinschaft (Te386/12-1). P. B. and H. J. W. Z. thank the Nederlandse organisatie voor Wetenschappelijk Onderzoek (NWO) for financial support. A. Z. acknowledges the Swedish Research Council (Vetenskapsradet) for the Tailspin project support.

Electronic Supplementary Material: Supplementary material (the characterization of instabilities as well as spatially resolved nanoprobe measurements) is available in the online version of this article at https://doi.org/10.1007/s12274-019-2425-5.

References

[1] de Heer, W. A.; Berger, C.; Ruan, M.; Sprinkle, M.; Li, X. B.; Hu, Y. K.; Zhang, B. Q.; Hankinson, J.; Conrad, E. Large area and structured epitaxial graphene produced by confinement controlled sublimation of silicon carbide. *Proc. Natl. Acad. Sci. USA* **2011**, *108*, 16900–16905.

[2] Emtsev, K. V.; Bostwick, A.; Horn, K.; Jobst, J.; Kellogg, G. L.; Ley, L.; McChesney, J. L.; Ohta, T.; Reshanov, S. A.; Röhrl, J. et al. Towards wafer-size graphene layers by atmospheric pressure graphitization of silicon carbide. *Nat. Mat.* **2009**, *8*, 203–207.

[3] Kruskopf, M.; Pakdehi, D. M.; Pierz, K.; Wundrack, S.; Stosch, R.; Dziomba, T.; Götz, M.; Baringhaus, J.; Aprojanz, J.; Tegenkamp, C. et al. Comeback of epitaxial graphene for electronics: Large-area growth of bilayer-free graphene on SiC. *2D Mater.* **2016**, *3*, 041002.

[4] Yang, Y. F.; Cheng, G. J.; Mende, P.; Calizo, I. G.; Feenstra, R. M.; Chuang, C.; Liu, C. W.; Liu, C. I.; Jones, G. R.; Hight Walker, A. R. et al. Epitaxial graphene homogeneity and quantum Hall effect in millimeter-scale devices. *Carbon* **2017**, *115*, 229–236.

[5] Virojanadara, C.; Yakimova, R.; Zakharov, A. A.; Johansson, L. I. Large homogeneous mono-/bi-layer graphene on 6H-SiC(0001) and buffer layer elimination. *J. Phys. D: Appl. Phys.* **2010**, *43*, 374010.

[6] Sprinkle, M.; Ruan, M.; Hu, Y.; Hankinson, J.; Rubio-Roy, M.; Zhang, B.; Wu, X.; Berger, C.; de Heer, W. A. Scalable templated growth of graphene nanoribbons on SiC. *Nat. Nanotechnol.* **2010**, *5*, 727–731.

[7] Baringhaus, J.; Ruan, M.; Edler, F.; Tejeda, A.; Sicot, M.; Taleb-Ibrahimi, A.; Li, A. P.; Jiang, Z. G.; Conrad, E. H.; Berger, C. et al. Exceptional ballistic transport in epitaxial graphene nanoribbons. *Nature* **2014**, *506*, 349–354.

[8] Zakharov, A. A.; Vinogradov, N. A.; Aprojanz, J.; Nguyen, T. T. N.; Tegenkamp, C.; Struzzi, C.; Iakimov, T.; Yakimova, R.; Jokubavicius, V. Wafer scale growth and characterization of edge specific graphene nanoribbons for nanoelectronics. *ACS Appl. Nano Mater.* **2019**, *2*, 156–162.

[9] Aprojanz, J.; Power, S. R.; Bampoulis, P.; Roche, S.; Jauho, A. P.; Zandvliet, H. J. W.; Zakharov, A. A.; Tegenkamp, C. Ballistic tracks in

graphene nanoribbons. *Nat*. *Commun*. **2018**, *9*, 4426.
[10] Ienaga, K.; Iimori, T.; Yaji, K.; Miyamachi, T.; Nakashima, S.; Takahashi, Y.; Fukuma, K.; Hayashi, S.; Kajiwara, T.; Visikovskiy, A. et al. Modulation of electron-phonon coupling in one-dimensionally nanorippled graphene on a macrofacet of 6H-SiC. *Nano Lett*. **2017**, *17*, 3527–3532.
[11] Palacio, I.; Celis, A.; Nair, M. N.; Gloter, A.; Zobelli, A.; Sicot, M.; Malterre, D.; Nevius, M. S.; de Heer, W. A.; Berger, C. et al. Atomic structure of epitaxial graphene sidewall nanoribbons: Flat graphene, miniribbons, and the confinement gap. *Nano Lett*. **2015**, *15*, 182–189.
[12] Bampoulis, P.; van Bremen, R.; Yao, Q. R.; Poelsema, B.; Zandvliet, H. J. W.; Sotthewes, K. Defect dominated charge transport and fermi level pinning in MoS_2/metal contacts. *ACS Appl*. *Mater*. *Interfaces* **2017**, *9*, 19278–19286.
[13] Bampoulis, P.; Sotthewes, K.; Siekman, M. H.; Zandvliet, H. J. W. Local conduction in $Mo_xW_{1-x}Se_2$: The role of stacking faults, defects, and alloying. *ACS Appl*. *Mater*. *Interfaces* **2018**, *10*, 13218–13225.
[14] Nowakowski, K.; Zandvliet, H. J. W.; Bampoulis, P. Barrier inhomogeneities in atomic contacts on WS_2. *Nano Lett*. **2019**, *19*, 1190–1196.
[15] Jokubavicius, V.; Yazdi, G. R.; Ivanov, I. G.; Niu, Y. R.; Zakharov, A.; Iakimov, T.; Syväjärvi, M.; Yakimova, R. Surface engineering of SiC via sublimation etching. *Appl*. *Surf*. *Sci*. **2016**, *390*, 816–822.
[16] Vodakov, Y. A.; Roenkov, A. D.; Ramm, M. G.; Mokhov, E. N.; Makarov, Y. N. Use of Ta-container for sublimation growth and doping of SiC bulk crystals and epitaxial layers. *Phys*. *Status Solidi B* **1997**, *202*, 177–200.
[17] Stöhr, A.; Baringhaus, J.; Aprojanz, J.; Link, S.; Tegenkamp, C.; Niu, Y. R.; Zakharov, A. A.; Chen, C. Y.; Avila, J.; Asensio, M. C. et al. Graphene ribbon growth on structured silicon carbide. *Ann*. *Phys*. **2017**, *529*, 1700052.
[18] Baringhaus, J.; Aprojanz, J.; Wiegand, J.; Laube, D.; Halbauer, M.; Hübner, J.; Oestreich, M.; Tegenkamp, C. Growth and characterization of sidewall graphene nanoribbons. *Appl*. *Phys*. *Lett*. **2015**, *106*, 043109.
[19] Riedl, C.; Coletti, C.; Starke, U. Structural and electronic properties of epitaxial graphene on SiC(0001): A review of growth, characterization, transfer doping and hydrogen intercalation. *J*. *Phys*. *D*: *Appl*. *Phys*. **2010**, *43*, 374009.
[20] Carpick, R. W.; Salmeron, M. Scratching the surface: Fundamental investigations of tribology with atomic force microscopy. *Chem*. *Rev*. **1997**, *97*, 1163–1194.
[21] Hunley, D. P.; Flynn, T. J.; Dodson, T.; Sundararajan, A.; Boland, M. J.; Strachan, D. R. Friction, adhesion, and elasticity of graphene edges. *Phys*. *Rev*. *B* **2013**, *87*, 035417.
[22] Borovikov, V.; Zangwill, A. Step-edge instability during epitaxial growth of graphene from SiC(0001). *Phys*. *Rev*. *B* **2009**, *80*, 121406.
[23] Allain, A.; Kang, J. H.; Banerjee, K.; Kis, A. Electrical contacts to two-dimensional semiconductors. *Nat*. *Mater*. **2015**, *14*, 1195–1205.
[24] Yu, L. L.; Lee, Y. H.; Ling, X.; Santos, E. J. G.; Shin, Y. C.; Lin, Y. X.; Dubey, M.; Kaxiras, E.; Kong, J.; Wang, H. et al. Graphene/MoS_2 hybrid technology for large-scale two-dimensional electronics. *Nano Lett*. **2014**, *14*, 3055–3063.
[25] Byun, K. E.; Chung, H. J.; Lee, J.; Yang, H.; Song, H. J.; Heo, J.; Seo, D. H.; Park, S.; Hwang, S. W.; Yoo, I. et al. Graphene for true ohmic contact at metal-semiconductor junctions. *Nano Lett*. **2013**, *13*, 4001–4005.
[26] Guo, Y. Z.; Liu, D. M.; Robertson, J. 3D behavior of schottky barriers of 2D transition-metal dichalcogenides. *ACS Appl*. *Mater*. *Interfaces* **2015**, *7*, 25709–25715.
[27] Miccoli, I.; Aprojanz, J.; Baringhaus, J.; Lichtenstein, T.; Galves, L. A.; Lopes, J. M. J.; Tegenkamp, C. Quasi-free-standing bilayer graphene nanoribbons probed by electronic transport. *Appl*. *Phys*. *Lett*. **2017**, *110*, 051601.
[28] Baringhaus, J.; Settnes, M.; Aprojanz, J.; Power, S. R.; Jauho, A. P.; Tegenkamp, C. Electron interference in ballistic graphene nanoconstrictions. *Phys*. *Rev*. *Lett*. **2016**, *116*, 186602.
[29] Aprojanz, J.; Miccoli, I.; Baringhaus, J.; Tegenkamp, C. 1D ballistic transport channel probed by invasive and non-invasive contacts. *Appl*. *Phys*. *Lett*. **2018**, *113*, 191602.
[30] Miccoli, I.; Edler, F.; Pfnür, H.; Tegenkamp, C. The 100th anniversary of the four-point probe technique: The role of probe geometries in isotropic and anisotropic systems. *J*. *Phys*.: *Condens*. *Matter* **2015**, *27*, 223201.
[31] Momeni Pakdehi, D.; Aprojanz, J.; Sinterhauf, A.; Pierz, K.; Kruskopf, M.; Willke, P.; Baringhaus, J.; Stöckmann, J. P.; Traeger, G. A.; Hohls, F. et al. Minimum resistance anisotropy of epitaxial graphene on SiC. *ACS Appl*. *Mater*. *Interfaces* **2018**, *10*, 6039–6045.
[32] Datta, S. *Electronic Transport in Mesoscopic Systems*; Cambridge University Press: Cambridge, 1995.
[33] Degawa, M.; Thürmer, K.; Morishima, I.; Minoda, H.; Yagi, K.; Williams, E. D. Initial stage of in-phase step wandering on Si(111) vicinal surfaces. *Surf*. *Sci*. **2001**, *487*, 171–179.
[34] Nevius, M. S.; Wang, F.; Mathieu, C.; Barrett, N.; Sala, A.; Mente, T. O.; Locatelli, A.; Conrad, E. H. The bottom-up growth of edge specific graphene nanoribbons. *Nano Lett*. **2014**, *14*, 6080–6086.
[35] Ming, F.; Zangwill, A. Model and simulations of the epitaxial growth of graphene on non-planar 6H-SiC surfaces. *J*. *Phys*. *D*: *Appl*. *Phys*. **2012**, *45*, 154007.